

Identifying Novel Lithium Superionic Conductors Using a High-Throughput Screening Model Based on Structural Parameters

Bo Xiao, Xiaohan Zhang, Liangliang Xu, Xianyong Wu, Ju Li, and Zhongfang Chen*

As the key component in solid-state batteries, Li superionic conductors ought to exhibit high ionic conductivities ($>10^{-4}$ S cm $^{-1}$) at room temperature (σ_{RT}). However, identifying such materials is a grand challenge due to the limited number of known candidates and the difficulty of predicting σ_{RT} with both efficiency and accuracy. Herein, a high-throughput screening model is developed that requires only two easily accessible parameters: the diameter of Li-ion diffusion path (D_{path}) and the dimension of Li-ion network (D_{Li}). This model successfully identifies Li superionic conductors from 132 experimentally available Li-ion conductors. Using this approach, 13 new candidates are screened out of the 21 686 Li-containing materials from the Materials Project, and their Li superionic conductivity is confirmed by first-principle molecular dynamics simulations. Notably, two N-containing materials (i.e., $\text{Li}_{6.5}\text{Ta}_{0.5}\text{W}_{0.5}\text{N}_4$ and $\text{Li}_{6.5}\text{Nb}_{0.5}\text{W}_{0.5}\text{N}_4$) are identified, enriching the rare N-based Li superionic conductor family, while $\text{Li}_2\text{Mo}_3\text{S}_4$ achieves the highest conductivity of 6.24×10^{-2} S cm $^{-1}$ due to its unique structure of interconnected Mo_6O_8 clusters, providing a robust and optimal diffusion path. $\text{Li}_{6.5}\text{Ta}_{0.5}\text{W}_{0.5}\text{N}_4$, $\text{Li}_{6.5}\text{Nb}_{0.5}\text{W}_{0.5}\text{N}_4$, and Li_7PSe_6 have been identified as promising solid-state electrolytes for use at the anode interface for the solid-state Li-ion batteries, while $\text{Li}_{10}\text{X}(\text{PS}_6)_2$ ($\text{X} = \text{Si}, \text{Ge}, \text{or Sn}$), $\text{Li}_2\text{Mn}_{0.75}\text{Ta}_{0.5}\text{Sn}_{0.5}\text{S}_4$, and $\text{Li}_2\text{Zn}_{0.5}\text{TaS}_4$ are suitable for the cathode interface. This work not only proposes a highly effective and accurate screening model for exploring Li superionic conductors but also provides several new frameworks for designing systems with ultrahigh σ_{RT} values.

1. Introduction

Li-ion batteries (LIBs) have been indispensable in powering electronics, electric vehicles, and large-scale energy storage systems.^[1,2] However, the widespread use of toxic and flammable organic liquid electrolytes in commercial LIBs poses significant safety risks. Moreover, these liquid electrolytes are generally incompatible with high-capacity electrode materials, such as Li metal or alloys, limiting the achievable energy density. To address these challenges, solid-state electrolytes (SSEs) have emerged as a promising alternative, enabling the development of all-solid-state batteries (SSBs) with enhanced energy density, improved safety, and longer cycling life.^[3–5]

Both academia and industry have focused intense research efforts on SSBs, typically utilizing polymeric or inorganic compounds as SSEs.^[6,7] To be effective, an ideal SSE should exhibit several key features: fast Li-ion conduction, low electronic conductivity, a wide electrochemical stability window, and robust mechanical stability. Among these features, ultrafast Li-ion conductivity at room temperature (σ_{RT}) is considered the most critical since all other properties can be fine-tuned by optimizing the structure and electronic characteristics of the electrode and electrolyte.^[8]

Despite their potential, the primary challenge in designing effective SSEs lies in their low σ_{RT} value, which is typically several orders of magnitude lower than that of liquid electrolyte ($\approx 10^{-2}$ S cm $^{-1}$ at room temperature), as illustrated in **Figure 1** and detailed in **Table S1** (Supporting Information). Traditionally, many Li-ion conductors (LICs) have been identified through “guess and check” or “trial and error” approaches. Based on their compositions and structures, these solid electrolytes could be classified into five major categories: i) oxides, such as LLTO-type $\text{Li}_x\text{La}_{2/3-x}\text{TiO}_3$,^[9] and garnet-type $\text{L}_5\text{La}_3\text{M}_2\text{O}_{12}$ ($\text{M} = \text{Ta}, \text{Nb}$);^[10,11] ii) sulfides, including $x\text{Li}_2\text{S}\cdot y\text{P}_2\text{S}_5$,^[12] and LGPS-type $\text{Li}_{10+x}\text{M}_{1+x}\text{P}_{2-x}\text{S}_{12}$ ($\text{M} = \text{Si}, \text{Ge}, \text{Sn}$);^[13,14] iii) phosphates, such as NASICON-type $\text{LiM}_2(\text{PO}_4)_3$ ($\text{M} = \text{Al}, \text{Ge}, \text{Hf}, \text{Zr}, \text{Ti}$);^[13,15] iv) nitrides and halides, such as Li_3N ,^[16] and LiMCl_6 ($\text{M} = \text{Ta}$ and/or Nb);^[17] v) LICs composed of multiple anions, such as

B. Xiao, X. Zhang

The Laboratory of Theoretical and Computational Chemistry
School of Chemistry and Chemical Engineering
Yantai University
Yantai 264005, China

B. Xiao, L. Xu, X. Wu, Z. Chen

Department of Chemistry
University of Puerto Rico
Rio Piedras Campus, San Juan 00931, Puerto Rico
E-mail: zhongfang.chen1@upr.edu

J. Li

Department of Nuclear Science and Engineering and Department of
Materials Science and Engineering
Massachusetts Institute of Technology
Cambridge, MA 02139, USA

The ORCID identification number(s) for the author(s) of this article can be found under <https://doi.org/10.1002/adfm.202507834>

DOI: 10.1002/adfm.202507834

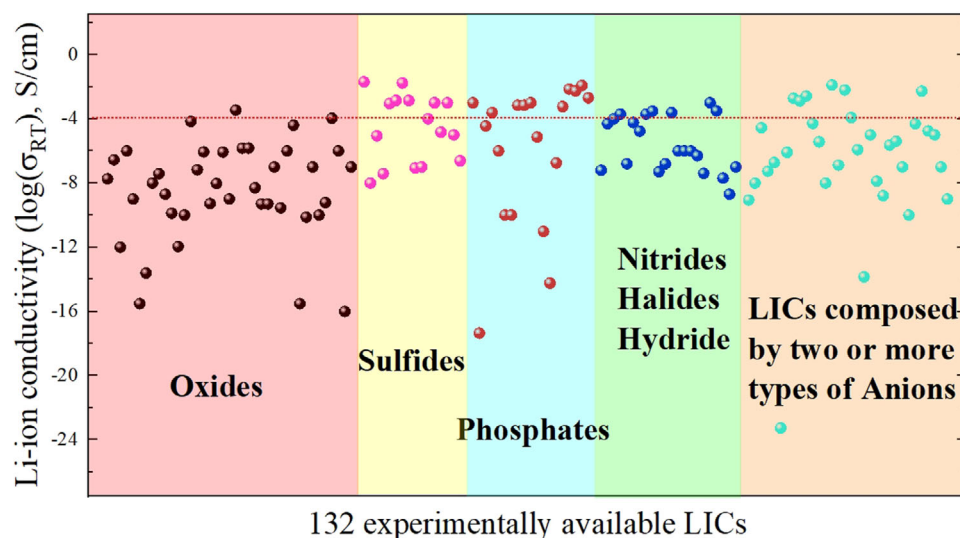


Figure 1. σ_{RT} values for 132 experimentally available LICs.

halide–sulfides ($\text{Li}_6\text{PS}_5\text{X}$, X = halogen),^[18,19] and halide–oxides (such as Li_3OBr and Li_3OCl).^[20,21]

In contrast to the traditional “guess and check” or “trial and error” experimental methods, high-throughput screening has recently emerged as an efficient strategy to identify Li superionic conductors ($\sigma_{RT} > 10^{-4} \text{ S cm}^{-1}$).^[8,22–33] Despite its promise, these screening methods often suffer from low predictive accuracy, with only a small percentage of predicted materials being validated as Li superionic conductors through first-principle molecular dynamics (FPMD) simulations. This limitation stems primarily from deficiencies in the screening models and the scarcity of comprehensive training data.

To construct a highly accurate screening model for identifying potential Li superionic conductors, it is imperative to thoroughly understand the diffusion mechanisms of Li ions within LICs. According to the Arrhenius equation ($D = A\exp(-E_a/RT)$) and the Einstein relation ($D = \langle |r(t) - r(0)|^2 \rangle / 6t$), Li-ion diffusivity depends on the pre-exponential factor (A), the ion diffusion energy barrier (E_a), and the displacement of Li ions ($r(t)$) during MD simulation. However, calculating these parameters through first-principle simulations is computationally intensive, making it impractical for high-throughput screening.

As an alternative, several empirical methods have been developed to estimate the diffusion barrier (E_a) and diffusion coefficient (D) more efficiently, such as the bond valence method,^[22–24] pinball model,^[8,25] and the recently proposed composition-based machine learning method.^[26] In addition, several structural factors have been linked to Li-ion conductivity. i) Wang et al. revealed that a body-centered cubic S sublattice, which facilitates direct Li hopping between adjacent tetrahedral sites, is optimal for high ionic conductivity.^[27] A similar conclusion was drawn by Zhang et al. using unsupervised machine learning.^[28] These findings imply that the size (or chemical environment) of the Li-ion diffusion pathways must fall within certain ranges to achieve high conductivity. ii) He et al. proposed that fast diffusion in Li

superionic conductors occurs not via isolated Li-ion hopping, as typically observed in solids, rather through the concerted motion of multiple Li ions with low energy barriers,^[29] indicating that the connectivity of Li-ion network in LICs is crucial for determining ionic conductivity. iii) Using machine-learning models, Sendek et al. identified two key descriptors, namely Li–Li bond length and Li–anion distance, that govern the ionic conductivity of LICs.^[30–32] iv) Through high-throughput screening models, Muy et al. and He et al. showed that Li-ion vibration frequencies and enlarged Li sites enhance Li-ion conductivity.^[33,34] v) Wang et al. proposed using density of atomistic states to quantitatively characterize the closed energy levels among Li sites in Li superionic conductors.^[35] vi) By tuning the collective anion motion in halides, Liu et al. revealed that the bottleneck in the diffusion path could be opened to achieve high Li-ion conductivity,^[36] which highlights the importance of local space or the chemical environment around Li ions.

Despite these advantages, none of the existing approaches could reliably differentiate between known LICs with high ($>10^{-4} \text{ S cm}^{-1}$) and low ($<10^{-4} \text{ S cm}^{-1}$) σ_{RT} values. Furthermore, many methods are limited to specific types of LICs, such as those containing S, O, or a single type of anion, resulting in reduced predictive efficiency for unknown Li superionic conductors. Nonetheless, these studies have collectively highlighted two key factors influencing Li-ion conductivity: the diameter (or chemical environment) of Li-ion diffusion path (D_{path}), and the dimension of Li-ion network (D_{Li}). Consequently, an effective and accurate screening model could be developed by precisely characterizing D_{path} and D_{Li} within LICs.

In this study, we developed a high-throughput screening model based on the abovementioned two key structural factors – D_{path} and D_{Li} – to identify potential Li superionic conductors. The model’s efficiency and accuracy were validated by successfully recognizing known Li superionic conductors among 132 experimentally available LICs and 21 686 Li-containing materials from the Materials Project database.^[37] As a result, 13 new Li superionic conductors were identified, several of which exhibit

ultrafast ionic conductivity, entirely novel structural frameworks, and excellent compatibility with the Li metal.

2. Computational Methods

All the first-principle simulations in this work were performed using the Vienna Ab Initio Simulation Package.^[38,39] The Perdew–Burke–Ernzerhof (PBE) functional within the generalized gradient approximation was employed to describe electron–ion and electron–electron interactions.^[40,41] To calculate the ionic conductivity of Li ions at room temperature, FPMD simulations were conducted at five different temperatures (750, 900, 1150, 1300, and 1500 K), and their room-temperature ionic conductivities were obtained by extrapolation.^[42] We simulated large supercells (≈ 100 atoms) to minimize the effects of periodic boundary conditions. During FPMD simulations, a gamma-centered k -point was used, and the Nosé–Hoover thermostat was employed under the NVT ensemble.^[43] The time step was set to be 2 fs. Each FPMD simulation was carried out for a duration of 100–600 ps, unless otherwise specified, until the diffusivity converged with a relative standard deviation below 20%, which aligns with the accuracy range (≈ 20 –30%) proposed in a previous study.^[42] For example, in the case of $\text{Li}_2\text{Mo}_3\text{S}_4$, the total simulation time was 570 ps, including 100 ps each at 900, 1150, 1300, and 1500 K, and 170 ps at 750 K. The Li ionic conductivity at room temperature, the corresponding error bound, and the activation energy were calculated following the previously established method.^[42]

For some candidate materials identified by high-throughput screening, aliovalent substitution was employed to adjust their Li contents. First, one dopant was selected based on substitution probability.^[44] Then, the Supercell program^[45] was used to generate all the symmetrically distinct substitution structures, and their stabilities were roughly screened using electrostatic Ewald energies. The energy above hull (E_{hull}) values for the 10 most stable configurations were further evaluated using first-principle calculations to identify the thermodynamically favorable structures.

Additionally, for pristine $\text{Li}_2\text{Mo}_3\text{S}_4$, deep potential molecular dynamics (DPMD) simulations were carried out at room temperature using the DeepMD-kit interface^[46] within the LAMMPS package.^[47] The training set was constructed by randomly selecting 80% of FPMD trajectories at 300, 750, 900, 1150, 1300, and 1500 K, while the remaining 20% of trajectories at 300 K were reserved as the testing set. The neutral network was trained using the Adam stochastic gradient descent method.^[48] We adopted the “se_e2_a” descriptor, which is constructed from both angular and radial information of the atomic structures. The sizes of the embedding and fitting neural networks were set to be (25, 50, 100) and (240, 240, 240), respectively. The radius and smooth cutoff were set to 6.00 and 0.50 Å, respectively. The initial learning rate was set to be 0.001, and the final drop ended at 3.50×10^{-8} over the course of training.

The initial screening steps, including the selection of Li-containing materials with specific bandgaps, energy above hull, and elemental composition, and the calculations for dimension of Li-ion network, were carried out using Pymatgen.^[49] The Zeo++ program^[50,51] was employed to calculate the diameters of the Li-ion diffusion pathways and identify blocked Li-ion positions.

3. Results and Discussion

3.1. Compilation and Overview of LIC Dataset

To establish a comprehensive dataset for LICs, we compiled 132 experimentally validated materials covering a wide range of conductivity values. As shown in Figure 1 and detailed in Table S1 (Supporting Information), these materials represent nearly all known categories of LICs. The σ_{RT} of these materials spans an extensive range, from 10^{-24} to 10^{-2} S cm^{-1} , with $\approx 25\%$ exhibiting σ_{RT} values greater than 10^{-4} S cm^{-1} , a commonly accepted threshold for classifying Li-ion superionic conductors.^[52–54]

3.2. Calculating the D_{path}

As highlighted in the previous section, Li-ion conductivity is closely linked to the D_{path} as well as the D_{Li} . Thus, we first calculated the D_{path} values across the LICs.

3.2.1. Simple Estimation Using the Zeo++ Program

Since Li-ion diffusion primarily occurs along the sublattice of Li-ion network, the diffusion path could be approximated as the connections between Li-vacancy sites. With approximation in mind, to calculate D_{path} , we removed all Li ions from the LICs, and used the Zeo++ program for the analysis. The van der Waals (vdW) radii of anions provided by the Cambridge Crystallography Data Center (CCDC)^[55] were incorporated, ensuring that the bonding behavior (chemical environment) between Li ions and anions was accounted for in the D_{path} calculations.

As shown in Figure 2a, the D_{path} values of all 33 Li superionic conductors ($\sigma_{\text{RT}} > 10^{-4}$ S cm^{-1}) exceed 1.00 Å, except for $\text{Li}_4\text{BH}_{10}\text{N}_3$ and Li_3YCl_6 , which will be discussed later. In the case of LICs with low σ_{RT} values ($< 10^{-4}$ S cm^{-1}), there are 23 materials also exhibiting D_{path} values greater than 1.00 Å. These results revealed that while D_{path} value higher than 1.00 Å is a necessary condition for high σ_{RT} ($> 10^{-4}$ S cm^{-1}), it is not sufficient on its own. Additional factors, beyond diffusion path size, also play a crucial role in determining ionic conductivity.

3.2.2. Correction Procedure for Materials with Nanopores

Although the initial D_{path} values obtained from our simple method are useful, they can sometimes be inaccurate and require careful correction, especially in materials with large nanopore structures. In such cases, Zeo++ considers both Li-vacancy sites and natural voids as part of Li-ion diffusion path, leading to an overestimation where the calculated D_{path} is essentially the diameter of the nanopore. For instance, in LiAlSiO_4 , which features a natural nanopore structure (Figure 3, left), the calculated D_{path} equals the nanopore diameter of 1.37 Å. However, since Li-ion diffusion must pass through its initial site within the material, which is an integral part of the diffusion path, the D_{path} value within such Li site should not exceed twice the difference between the averaged Li–anion bond length ($d_{\text{Li–Anion}}$) and the vdW radius of the anion (r_{Anion}). For example, the averaged Li–O bond

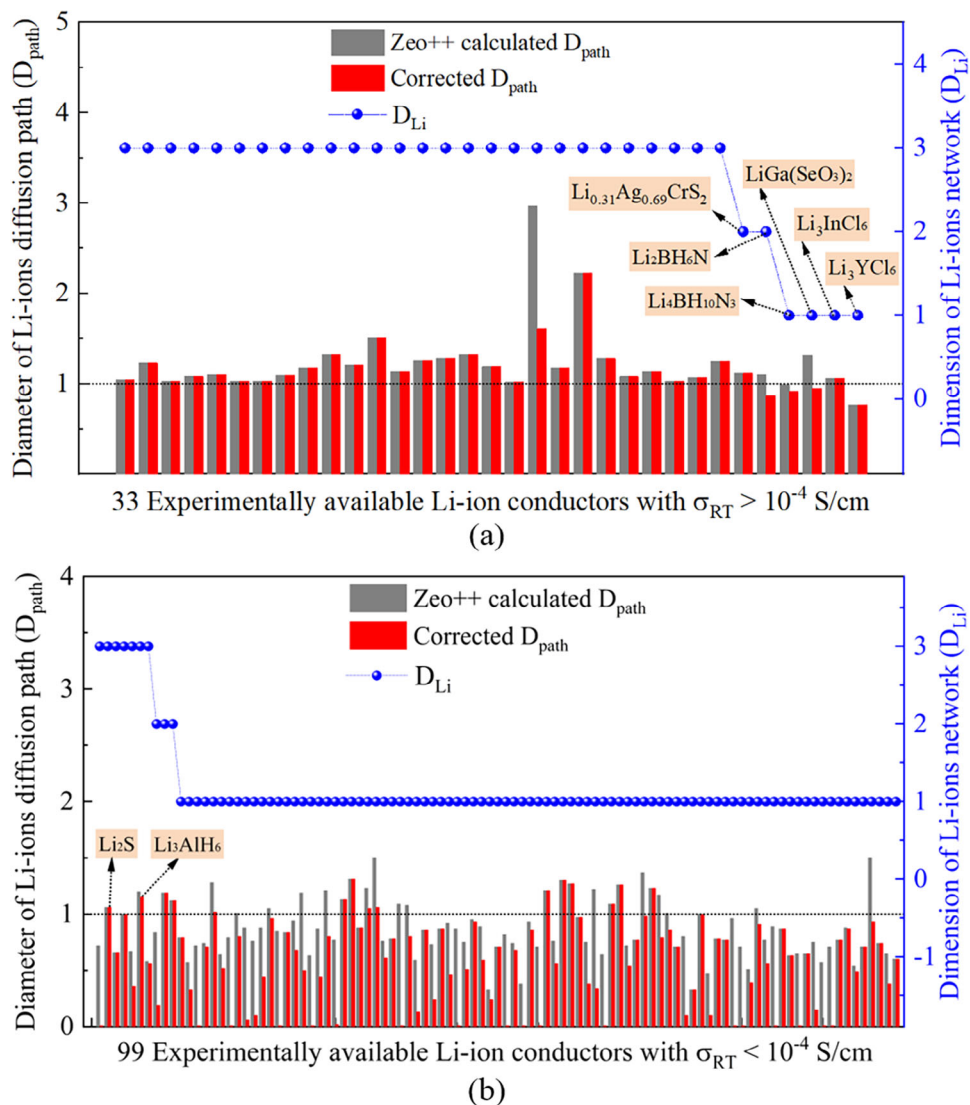


Figure 2. Comparison of D_{path} and D_{Li} values in a) fast and b) slow LICs.

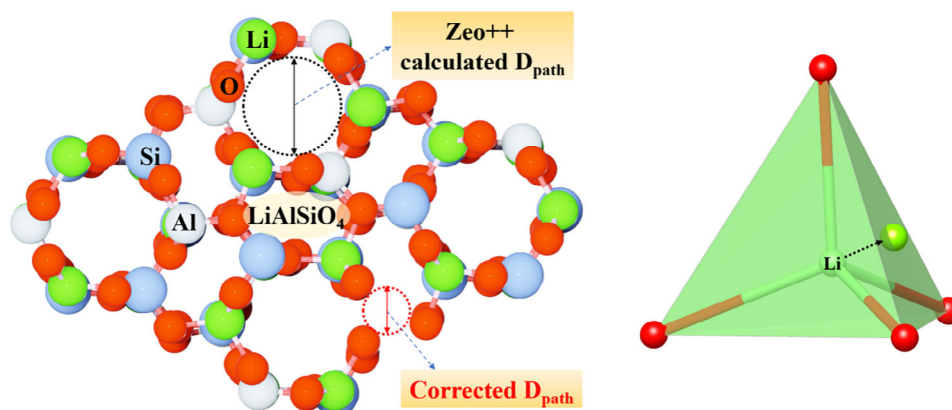


Figure 3. Schematic representation of the correction process for D_{path} values for LICs with nanopore structures.

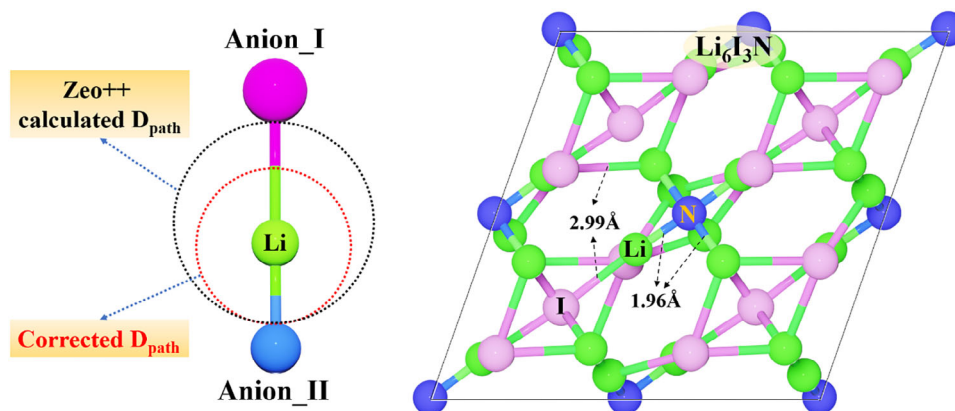


Figure 4. Schematic illustration of the correction process for D_{path} values in LICs containing two types of anions.

length in LiAlSiO_4 is 2.01 Å, indicating that the actual D_{path} value should be no greater than $2 \times (d_{\text{Li-O}} - r_{\text{O}}) = 0.98$ Å (with $r_{\text{O}} = 1.52$ Å). Moreover, the Li ion resides within an oxygen-containing tetrahedron, and must traverse an O_3 triangle during diffusion (Figure 3, right), where the Li–O distance is about 0.05 Å shorter than the average Li–O bond. In this regard, the actual D_{path} value for LiAlSiO_4 should be further reduced to not higher than 0.88 Å. Therefore, for LICs with large nanopores, the D_{path} values calculated by Zeo++ must be corrected: the actual D_{path} values should be less than $2 \times (d_{\text{Li-Anion}} - r_{\text{Anion}}) \times \alpha$, where α is the tolerance factor accounting for these structural nuances.

In most LICs, Li ions preferentially occupy tetrahedral (T) sites rather than octahedral (O) sites, and long-range Li-ion diffusion typically follows pathways such as $\text{T} \leftrightarrow \text{O} \leftrightarrow \text{T}$ or $\text{T} \leftrightarrow \text{T}$.^[27] Thus, we can assume that a Li ion resides at the center of a regular tetrahedron formed by four anions, as illustrated in Figure 3 (right). In this configuration, the $d_{\text{Li-Anion}}$ value is about 5% greater than half of the D_{path} value. Therefore, in this work, the correction factor α is set to 0.95.

Applying this correction, we identified overestimated D_{path} values in six LICs with large nanopores: $\text{LiAl}(\text{Si}_2\text{O}_5)_2$, LiAlSiO_4 , LiGaSiO_4 , $\text{LiZr}_2(\text{PO}_4)_3$, LiScP_2O_7 , and LiSbO_2 . After correction, the corrected D_{path} values for these materials fall below 1.00 Å. Furthermore, this correction procedure should also be extended to other LICs where the Li-ion coordination number exceeds three since most Li-ion diffusion involves crossing T sites. Thus, for these materials, the corrected D_{path} values should not exceed $2 \times (d_{\text{Li-Anion}} - r_{\text{Anion}}) \times 0.95$.

3.2.3. Correction Procedure for Materials with Two or More Anions

In materials containing two types of anions, accurate determination of Li-ion diffusion paths requires careful correction due to discrepancies that arose between the Li site positions identified by Zeo++ and the actual Li sites within the material. As illustrated in Figure 4 (left), the Li site identified by Zeo++ is located centrally between Anion_I and Anion_II, resulting in a calculated D_{path} value approximately equal to $(d_{\text{Li-Anion}_I} - r_{\text{Anion}_I} + d_{\text{Li-Anion}_II} - r_{\text{Anion}_II})$. However, the actual Li site depends on the specific chemical properties of Anion_I and Anion_II, meaning the true D_{path} should be lower

than the minimum of $2 \times (d_{\text{Li-Anion}_I} - r_{\text{Anion}_I}) \times 0.95$ and $2 \times (d_{\text{Li-Anion}_II} - r_{\text{Anion}_II}) \times 0.95$. This overestimation becomes particularly pronounced when the two anions have significantly different vdW radii. The most common anions in LICs – O, N, P, S, Cl, Br, and I – have vdW radii (r_{Anion}) of 1.52, 1.55, 1.80, 1.80, 1.75, 1.85, and 1.98 Å, respectively. Consequently, D_{path} values for LICs containing pairs of anions, such as O or N with P, S, Cl, Br, or I, are often overestimated and should be carefully corrected.

Accurate correction of D_{path} values is crucial for LICs containing multiple types of anions to avoid overestimating Li-ion conductivity. Taking $\text{Li}_6\text{I}_3\text{N}$ as an example (Figure 4, right), the Li–I and Li–N bond lengths are 2.99 and 1.96 Å, respectively, with a Zeo++ calculated D_{path} value of 1.18 Å. However, the actual D_{path} value for $\text{Li}_6\text{I}_3\text{N}$ should be lower, calculated as $2 \times (d_{\text{Li-N}} - r_{\text{N}}) \times 0.95 = 0.78$ Å. A similar correction procedure was applied to other LICs containing two types of anions. As a result, five LICs, namely, $\text{Li}_6\text{I}_3\text{N}$, Li_5NCl_2 , $\text{Li}_9\text{S}_3\text{N}$, $\text{Li}_6\text{Br}_3\text{N}$, and $\text{Li}_2\text{B}_3\text{O}_4\text{F}_3$, with original D_{path} values (obtained by Zeo++) exceeding 1.00 Å, were excluded from the list of Li superionic conductors due to their corrected D_{path} values being below 1.00 Å. Note that this correction process should also be applied to LICs containing more than two types of anions, though such materials are rare in experimental studies.

3.2.4. Correction Procedure for Materials Containing Immobile Li Ions

Finally, it is important to recognize that the chemical environment of Li ions in LICs can vary, leading to different ionic conductivities for different types of Li ions. As mentioned above, Li ions with a local D_{path} value greater than 1.00 Å are likely to exhibit fast diffusion, while those with $D_{\text{path}} < 1.00$ Å are expected to have lower ionic conductivities. Therefore, it is crucial not to remove all the Li ions from LICs during D_{path} calculations using Zeo++, as some of the Li ions may not be mobile. One approach to determine the local D_{path} value for each Li ion is through the bond-length-based correction method described in Figures 3 and 4. However, this method assumes that Li ions reside at the center of a regular tetrahedron formed by four anions, which may not fully capture the actual environment of Li ions in LICs.

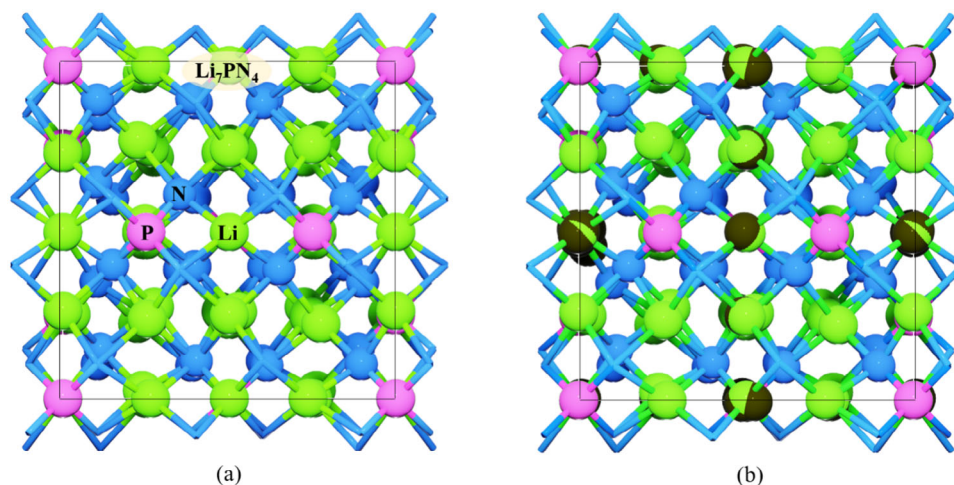


Figure 5. Structural representation of Li_7PN_4 , illustrating the configurations a) with and b) without blocked Li ions (depicted as black spheres).

To address the inaccuracies in identifying blocked Li-ion sites with low diffusion potential (local $D_{\text{path}} < 1.00 \text{ \AA}$), we performed Monte Carlo (MC) simulations as implanted in Zeo++. In this approach, all Li ions were initially removed from the LICs, and 20 blocking spheres, with diameters ranging from 0.60 to 1.00 \AA , were used to pinpoint the exact locations of blocked Li sites. Li ions positioned within 1.00 \AA of these blocked sites were classified as having low ionic conductivity. The D_{path} value was then corrected by incorporating these blocked Li ions as part of the anion framework.

For example, in Li_7PN_4 ($\sigma_{\text{RT}} < 10^{-4} \text{ S cm}^{-1}$, **Figure 5**), the initially calculated D_{path} value using Zeo++ was 1.01 \AA . Among the 56 Li ions in the structure, 13 blocked Li ions were identified through MC simulations (represented as black spheres in **Figure 5b**). An additional 35 Li ions with local D_{path} values lower than 1.00 \AA were identified using the bond-length-based correction method. After removing the remaining eight Li ions from the structure, the recalculated D_{path} value dropped to 0.80 \AA , below the 1.00 \AA threshold typically required for classification as Li superionic conductor.

In summary, the D_{path} values obtained by Zeo++ require careful correction, particularly for LICs with large nanopores, those composed of two or more types of anions with significantly different vdW radii, or materials containing immobile Li ions. Using a corrected $D_{\text{path}} > 1.00 \text{ \AA}$ as the criterion, 28 out of 33 Li superionic conductors were successfully identified, while 85 LICs were excluded, as shown in **Figure 2**. Thus, while the D_{path} value is a necessary criterion for identifying Li superionic conductors, it alone is insufficient for complete classification.

3.3. Examining the D_{Li}

So far, we have determined the size of the diffusion path in LICs, but another key factor determining the Li-ion conductivity is the connectivity of Li-ion network, which can be easily quantified by calculating the D_{Li} value. However, it is important to note that such Li-ion networks consist only of movable Li ions; blocked Li

ions, with local D_{path} values below 1.00 \AA , should be excluded from the network.

To illustrate the importance of D_{Li} value, we examined the example of Li_4GeS_4 ($\sigma_{\text{RT}} = 2.00 \times 10^{-7} \text{ S cm}^{-1}$, **Figure 6**). When blocked Li ions are not considered, the calculated D_{Li} value is 3 initially. The Zeo++ calculated blocked spheres, represented as black spheres, are located near some Li ions, indicating they are blocked. Notably, the bond-length-based correction method could not identify these blocked Li ions. After removing them, the D_{Li} value decreases to 2.

Using this improved approach, we calculated the D_{Li} values for all 132 LICs (**Figure 2**). Among the 33 Li superionic conductors, 27 exhibit a 3D Li-ion network with a Li–Li cutoff distance of 4.05 \AA . By contrast, 91 out of the remaining 99 LICs display 1D or 2D Li-ion networks. Therefore, we concluded that $D_{\text{Li}} = 3$ is a key criterion for identifying Li superionic conductors (for layered structures, $D_{\text{Li}} = 2$; see the discussions about $\text{Li}_{0.31}\text{Ag}_{0.69}\text{CrS}_2$ in **Section 3.4**).

3.4. Evaluation of Screening Model Accuracy and Analysis of Unidentified LICs

Based on the discussions above, the accuracy of our screening model was evaluated by applying two key criteria for identifying Li superionic conductors: a corrected $D_{\text{path}} > 1.00 \text{ \AA}$ and a D_{Li} value of 3 (**Figure 2**). Of the 132 LICs evaluated, only eight out were misclassified: $\text{Li}_{0.31}\text{Ag}_{0.69}\text{CrS}_2$, $\text{Li}_2\text{BH}_6\text{N}$, $\text{Li}_4\text{BH}_{10}\text{N}_3$, $\text{LiGa}(\text{SeO}_3)_2$, Li_3InCl_6 , and Li_3YCl_6 were incorrectly categorized as low LICs, while Li_2S and Li_3AlH_6 were wrongly identified as Li-ion superconductors. This result demonstrates the high accuracy of our screening model. Next, we analyze the structural properties of these eight “negative” materials.

$\text{Li}_{0.31}\text{Ag}_{0.69}\text{CrS}_2$ ($D_{\text{path}} = 1.12 \text{ \AA}$) is a layered structure with Li ions in the interlayer region,^[56] forming a 2D Li-ion network. Given the ultrahigh σ_{RT} value ($1.96 \times 10^{-2} \text{ S cm}^{-1}$), we suggest that layered LICs with $D_{\text{path}} > 1.00 \text{ \AA}$ and $D_{\text{Li}} = 2$ may also be potential Li superionic conductors.

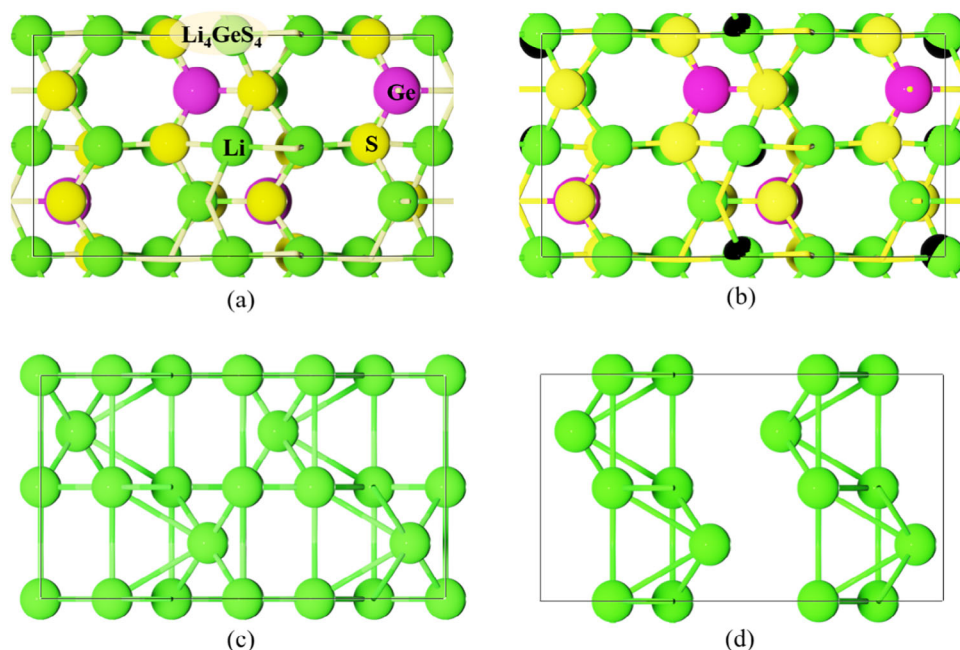


Figure 6. a,b) Structures of Li_4GeS_4 and c,d) their corresponding Li-ion networks, with and without the inclusion of blocked Li ions (shown as black spheres).

In the case of Li_2S ($D_{\text{path}} = 1.06 \text{ \AA}$, $D_{\text{Li}} = 3$, $\sigma_{\text{RT}} = 1 \times 10^{-5} \text{ S cm}^{-1}$), previous studies revealed that the highly symmetric face-centered cubic (fcc, such as Li_2S) S sublattice contributes to a high Li-ion diffusion barrier from T-site to O-site, resulting in low ionic conductivity.^[27] However, since materials with highly symmetric fcc S sublattices are rare, this condition will not be considered in our screening process.

$\text{Li}_2\text{BH}_6\text{N}$ ($D_{\text{path}} = 0.87 \text{ \AA}$, $D_{\text{Li}} = 2$, $\sigma_{\text{RT}} = 1.00 \times 10^{-4} \text{ S cm}^{-1}$), $\text{Li}_4\text{BH}_{10}\text{N}_3$ ($D_{\text{path}} = 0.92 \text{ \AA}$, $D_{\text{Li}} = 1$, $\sigma_{\text{RT}} = 2.00 \times 10^{-4} \text{ S cm}^{-1}$), and Li_3AlH_6 ($D_{\text{path}} = 1.15 \text{ \AA}$, $D_{\text{Li}} = 3$, $\sigma_{\text{RT}} = 1.00 \times 10^{-7} \text{ S cm}^{-1}$) all feature Li ions coordinated with the MH_4 units ($M = \text{B}$ or Al). The Li–H bond lengths in these materials are 2.00, 2.37, and 1.95 \AA , respectively, which are significantly longer than that in LiH (1.60 \AA), indicating their weak interaction strengths. As a result, it is likely that the MH_4 units move during Li-ion diffusion, making structural parameters such as D_{path} difficult to determine accurately. Therefore, such materials should be excluded from our screening model.

$\text{LiGa}(\text{SeO}_3)_2$ was recently identified as a Li superionic conductor,^[57] but our results indicate a relatively low D_{path} value (0.95 \AA) and 1D Li-ion network. Its σ_{RT} value of $1.10 \times 10^{-4} \text{ S cm}^{-1}$ is very close to the threshold for fast and slow LICs ($1.00 \times 10^{-4} \text{ S cm}^{-1}$), suggesting that the failure to recognize $\text{LiGa}(\text{SeO}_3)_2$ as a Li superionic conductor may be due to the inherent margin of error within our screening model.

Li_3InCl_6 and Li_3YCl_6 are representatives of Li_3MX_6 -type halide electrolytes, which exhibit high Li ionic conductivity of about $1.00 \times 10^{-3} \text{ S cm}^{-1}$ at room temperature. However, our simulations revealed that Li-ion diffusion was fully blocked in these structures, indicating a key limitation of our current screening model for this class of compounds. In our model, the Li-

ion diffusion path size is mainly determined by the vdW radii of the anions, which inherently assumes these radii could adequately capture the interaction strength between Li and its surrounding anions. This approximation has proven effective for a broad range of LICs, as demonstrated by the successful identification of various sulfide and oxide superionic phases. However, as discussed in previous studies,^[58] Li_3MX_6 -type halides possess layered structures similar to the well-established layered transition-metal oxides, where interlayer Coulomb interactions significantly influence the diffusion of Li ions. In such systems, the charge of the anions becomes a dominant factor that the vdW-based model does not account for. For example, the vdW radii of S and Cl are similar (1.80 vs 1.75 \AA), yet Cl^- has higher electronegativity and lower valence compared to S^{2-} . According to our model, this should not favor an enhanced Li-ion diffusion. Yet, in Li_3YCl_6 ($D_{\text{path}} = 0.77 \text{ \AA}$), a fast Li-ion diffusion was observed, which is primarily driven by weaker Coulomb interactions between Li^+ and Cl^- ,^[59] a factor not accounted for in our current descriptor. Thus, our model underestimates the diffusion capacity of Li_3MX_6 -type halides. To correctly identify this type of Li superionic halides, a significantly lower D_{path} threshold or an improved descriptor incorporating electrostatic interactions, may be necessary in future screening studies.

To summarize, our screening model demonstrates high accuracy in predicting Li superionic conductors, successfully categorizing 124 materials out of 132 experimentally available LICs as either low or superionic conductors. However, as discussed above, we recognize that the model does not account for all types of LICs, particularly those with unique structural characteristics.

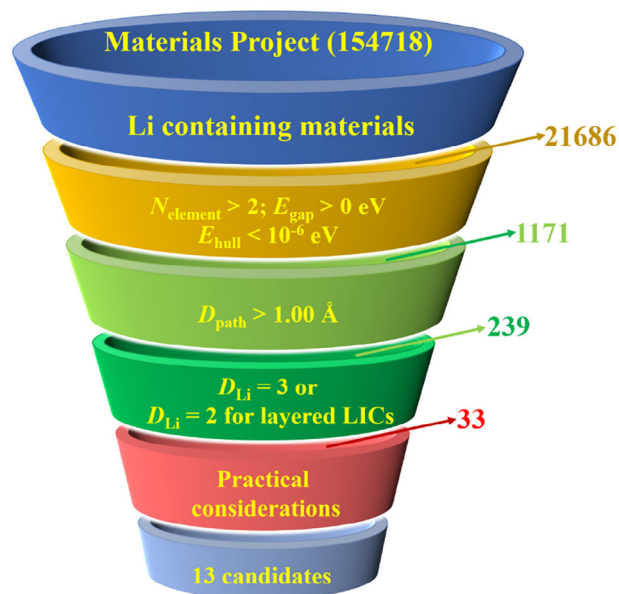


Figure 7. High-throughput screening steps for identifying Li superionic conductors.

3.5. Screening Li-Ion Superionic Conductors from Materials Project Database

Building on the success of our model, we extended our search for potential Li superionic conductors using the Materials Project database. The screening process involved several key steps (Figure 7): i, ii) materials must contain Li ions and be composed of more than two elements, with bandgap values greater than 0 eV and energy above hull values below 10^{-6} eV; iii) the corrected D_{path} values must exceed 1.00 Å; iv) D_{Li} values must equal to 3 or 2 for layered LICs; v) practical considerations were applied to exclude materials containing toxic and expensive elements (such as Be, As, Sb, Au, Pt, and lanthanide and actinide elements), as well as those containing MH_4 units, Li_3MX_6 -type halides or already known Li superionic conductors.

Note that our screening model is highly sensitive to the vdW radii of anions. For certain elements (e.g., Be, B, Al, Ca, Sc, Ti, V, Cr, Mn, Fe, Co, Ge, and elements with large atomic numbers), vdW radii are not well-defined in the CCDC,^[49] with only the default value of 2.00 Å available. As a result, our screening model could not predict the σ_{RT} values for LICs containing these anions well. Fortunately, the vdW radii of widely present anions (such as H, N, O, F, P, S, Cl, and I) are well-defined in the CCDC, allowing our screening model to cover the majority of LICs. This screening scheme identified 33 out of 21 686 LICs as potential Li superionic conductors (Table S2, Supporting Information). However, after accounting for practical factors, 16 candidates contain expensive or toxic elements, leaving with 17 viable options. Of these, four are already known, resulting in 13 newly predicted, previously unknown and practical Li-ion superionic conductors (Table 1).

Finally, we calculated the σ_{RT} values for the 13 identified candidates using FPMD simulations. Note that the D_{Li} value used in our high-throughput screening model may overestimate Li con-

tents in materials with fully occupied Li sites, which lack available hopping pathways. To address this issue, aliovalent substitution was used to reduce Li content and create mobile Li vacancies in such materials, thereby enhancing ionic conductivity (for pristine structures with native Li hopping sites, no substitution was applied, and their Li contents remain the same). Subsequent FPMD simulations confirmed that all the 13 candidates exhibit superionic behavior, further affirming the high accuracy of our screening model, as summarized in Table 1. The corresponding mean square displacement (MSD) curves and Arrhenius plots are shown in Figures S1 and S2 (Supporting Information), respectively. Following a previous study,^[42] the ballistic region at the initial stage and the poor linearity region at the terminal stage of the MSD curves were excluded from diffusivity calculations. In all cases, the linear regions of the MSD curves exhibited excellent linearity, with R^2 values exceeding 0.98.

The structures of all these 13 newly identified Li superionic conductors are shown in Figure S3 (Supporting Information). Several new material types were discovered, expanding the landscape of known LICs. For example, LICs with Si as the anions, such as $\text{Li}_{1.75}\text{Mg}_{0.875}\text{Hf}_{0.125}\text{Si}$ and $\text{Li}_{13}\text{Mg}_{0.5}\text{Hf}_{0.5}\text{Si}_4$, were identified for the first time as Li superionic conductors. However, because of the small bandgaps, these materials are likely mixed ionic electronic conductors, and may be used as high-rate electrode materials,^[60,61] rather than SSEs. Additionally, the previously reported $\text{Li}_{10}\text{X}(\text{PSe}_6)_2$ (X = Si, Ge, or Sn) Li superionic conductors were extended into $\text{Li}_{10}\text{X}(\text{PSe}_6)_2$ systems. Furthermore, the family of N-anion-based Li superionic conductors was enriched, such as $\text{Li}_{6.5}\text{Ta}_{0.5}\text{W}_{0.5}\text{N}_4$ and $\text{Li}_{6.5}\text{Nb}_{0.5}\text{W}_{0.5}\text{N}_4$. Their Li probability densities obtained from FPMD simulations at 900 K are shown in Figure 8a,b, respectively, which clearly show the 3D Li-ion diffusion path. Remarkably, the σ_{RT} value of $\text{Li}_2\text{Mo}_3\text{S}_4$ reaches $6.24 \times 10^{-2} \text{ S cm}^{-1}$, the highest among all 13 candidates. The structure of $\text{Li}_2\text{Mo}_3\text{S}_4$ is unique (Figure 8c), with Mo_6S_8 clusters connected by only two Mo–S bonds. This configuration forms a highly rigid 3D diffusion path, allowing for rapid Li-ion movement. This structural feature is similar to that of $\text{Li}_{0.31}\text{Ag}_{0.69}\text{CrS}_2$,^[56] a layered structure where the distance between adjacent CrS_2 layers is stabilized by Ag ions in the interlayer region, resulting in very high ionic conductivity ($1.96 \times 10^{-2} \text{ S cm}^{-1}$) at room temperature. The Li probability density in $\text{Li}_2\text{Mo}_3\text{S}_4$ (Figure 8d) confirms the 3D diffusion pathway at 900 K.

Note that our calculated D_{Li} value for $\text{Li}_2\text{Mo}_3\text{S}_4$ is 2, indicating a 2D Li-ion diffusion network at room temperature, despite its nonlayered structure. To verify this point, we performed FPMD simulations at 300 K for 1 ns. As shown in Figure S4 (Supporting Information), the MSD of Li ions along a direction is nearly negligible, which confirms the 2D nature of Li-ion diffusion. This is further supported by the 2D Li-ion network topology and Li probability density shown in Figure S5 (Supporting Information). In addition, the calculated Li ionic conductivity based on such extended room-temperature FPMD simulation is about $3.89 \times 10^{-2} \text{ S cm}^{-1}$, which agrees with the above result ($6.24 \times 10^{-2} \text{ S cm}^{-1}$) obtained by extrapolation.

To further verify the fast Li-ion diffusion in pristine $\text{Li}_2\text{Mo}_3\text{S}_4$, we performed long-timescale DPMD simulations for 40 ns. The deep potential model for the $\text{Li}_2\text{Mo}_3\text{S}_4$ system was trained using trajectories from FPMD simulations at 300, 750, 900, 1150, 1300,

Table 1. List of 13 newly predicted practical Li superionic conductors with the corresponding doped compositions, corrected D_{path} and D_{Li} values, E_{hull} values, σ_{RT} and error bound values, E_a , and bandgap values calculated by using PBE and Heyd–Scuseria–Ernzerhof-06 (HSE06) hybrid (in bracket) functionals.

MP-ID	Original composition	Doped composition	Corrected D_{path} [Å]	D_{Li}	E_{hull} [meV per atom]	σ_{RT} [mS cm ⁻¹]	Error bound (σ_{min} , σ_{max}) [mS cm ⁻¹]	E_a [meV]	Bandgap [eV]
1222572	Li ₇ Cu ₂ N ₃	Li ₇ Cu ₂ N ₃	1.19	3	0	21.80	[9.63, 49.33]	216 ± 20	0.32 (1.19)
685991	Li ₅ SiP ₃	Li _{4.75} Si _{0.75} V _{0.25} P ₃	1.32	3	42	0.50	[0.21, 1.18]	351 ± 21	0.64 (2.07)
1222798	Li ₁₄ MgSi ₄	Li ₁₃ Mg _{0.5} Hf _{0.5} Si ₄	1.30	3	49	2.70	[1.11, 6.57]	308 ± 22	0 (0.46)
721239	Li ₁₀ Ge(PSe ₆) ₂	Li ₁₀ Ge(PSe ₆) ₂	1.14	3	0	1.27	[0.49, 3.30]	314 ± 24	1.31 (2.27)
721252	Li ₁₀ Sn(PSe ₆) ₂	Li ₁₀ Sn(PSe ₆) ₂	1.15	3	0	1.40	[0.53, 3.65]	306 ± 24	1.37 (2.30)
721253	Li ₁₀ Si(PSe ₆) ₂	Li ₁₀ Si(PSe ₆) ₂	1.14	3	0	0.86	[0.40, 1.84]	329 ± 19	1.46 (2.46)
1211446	Li ₇ PSe ₆	Li ₇ PSe ₆	1.10	3	0	1.74	[0.73, 4.14]	309 ± 22	0.93 (1.79)
14753	Li ₇ TaN ₄	Li _{6.5} Ta _{0.5} W _{0.5} N ₄	1.03	3	15	0.13	[0.04, 0.45]	341 ± 30	3.00 (4.45)
14827	Li ₇ NbN ₄	Li _{6.5} Nb _{0.5} W _{0.5} N ₄	1.03	3	17	0.63	[0.18, 2.11]	287 ± 30	2.94 (4.44)
1105932	Li ₂ MgSi	Li _{1.75} Mg _{0.875} Hf _{0.125} Si	1.02	3	45	0.50	[0.21, 1.18]	351 ± 21	0 (0)
1105291	Li ₂ MnSnS ₄	Li ₂ Mn _{0.75} Ta _{0.5} Sn _{0.5} S ₄	1.02	3	61	17.02	[7.96, 36.41]	214 ± 19	1.00 (2.95)
555186	Li ₂ ZnSnS ₄	Li ₂ Zn _{0.5} Ta _{0.5} S ₄	1.04	3	42	0.21	[0.08, 0.54]	363 ± 23	1.57 (2.92)
675779	Li ₂ Mo ₃ S ₄	Li ₂ Mo ₃ S ₄	1.05	2	0	62.42	[19.45, 200.28]	134 ± 29	1.44 (2.24)

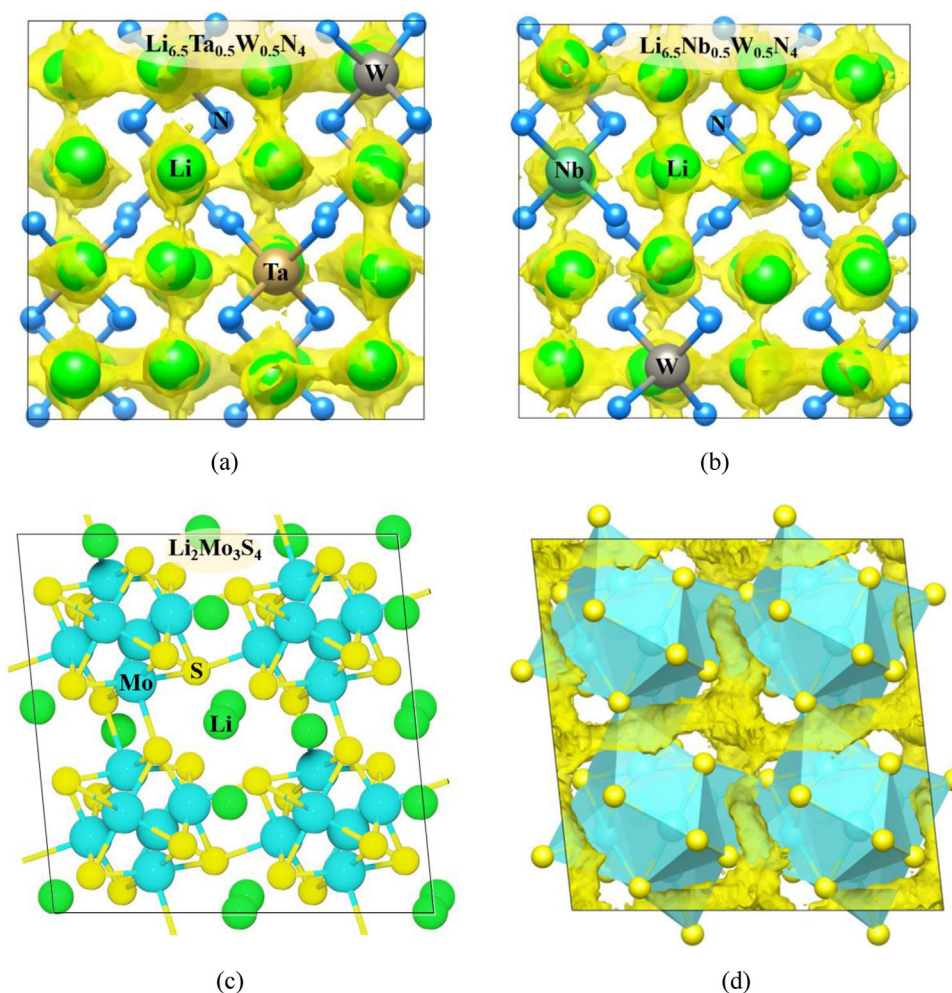


Figure 8. Li-ion probability densities for a) $\text{Li}_{6.5}\text{Ta}_{0.5}\text{W}_{0.5}\text{N}_4$, and b) $\text{Li}_{6.5}\text{Nb}_{0.5}\text{W}_{0.5}\text{N}_4$ from FPMD simulations at 900 K. c) The crystal structure of $\text{Li}_2\text{Mo}_3\text{S}_4$ and d) its corresponding Li-ion probability density at 900 K.

and 1500 K, as described above. The accuracy of the trained deep potential was validated by comparing energies and forces with FPMD simulations, as presented in Figure S6 (Supporting Information). The root mean square error for energy per atom and force per atom were found to be only 1.59×10^{-4} eV and 2.50×10^{-2} eV \AA^{-1} , respectively, which confirms the high fidelity of the deep potential model. Using this model, DPMD simulation was carried out at 300 K for 40 ns. The calculated σ_{RT} value reaches an impressive 1.60×10^{-2} S cm^{-1} , further confirming the ultrahigh ionic conductivity of $\text{Li}_2\text{Mo}_3\text{S}_4$.

3.5.1. Application as SSEs in Solid-State Li-Ion Batteries

Finally, we assessed the potential of using these 13 identified Li superionic conductors as SSEs in Li-ion solid-state batteries. It is well established that ideal SSEs should exhibit high Li-ion conductivity, low electronic conductivity, and high electrochemical stability at electrode interfaces.^[62]

To evaluate their suitability, we corrected the bandgap values initially obtained at the PBE level using the Heyd–Scuseria–Ernzerhof (HSE) functional,^[63] as presented in Table 1. Note that these corrected bandgap values only represent the upper bound of the electrochemical windows of SSEs.^[62] Additionally, to assess chemical stability under extreme conditions of Li chemical potential, we plotted their grand potential phase diagram.^[64] In doing so, we calculated the phase equilibria of each candidate at the anode (Li metal chemical potential μ_{Li}^0) and cathode ($\mu_{\text{Li}}^0 - 5$ eV corresponding to a charged high voltage, 5 V) limits, as listed in Table S3 (Supporting Information). Decomposition of a material at either electrode suggests incompatibility with that electrode. However, if the decomposed phases exhibit high Li ionic conductivity and low electronic conductivity, they are expected to form a passivating interphase layer at the SSE/electrode interphase, which can help stabilize the SSE.

The cases of $\text{Li}_{6.5}\text{Ta}_{0.5}\text{W}_{0.5}\text{N}_4$ and $\text{Li}_{6.5}\text{Nb}_{0.5}\text{W}_{0.5}\text{N}_4$ emerge as promising candidates for use with Li metal anodes, as the lithiation process is not feasible at 0 V. Although both of them may decompose into the most stable compounds Li_6WN_4 and Li_7MN_4 ($M = \text{Ta}$ or Nb) at 0 V, such decomposition processes are not favorable since the E_{hull} values of $\text{Li}_{6.5}\text{Ta}_{0.5}\text{W}_{0.5}\text{N}_4$ and $\text{Li}_{6.5}\text{Nb}_{0.5}\text{W}_{0.5}\text{N}_4$ are only 0.015 and 0.017 eV, respectively. Their large bandgap values (4.45 and 4.44 eV at the HSE level) further suggest they could serve as effective Li protection layers. Notably, to our knowledge, Li_3N is the only known N-based LIC that has demonstrated excellent performance as an interlayer in Li-ion solid-state batteries.^[65] Thus, $\text{Li}_{6.5}\text{Ta}_{0.5}\text{W}_{0.5}\text{N}_4$ and $\text{Li}_{6.5}\text{Nb}_{0.5}\text{W}_{0.5}\text{N}_4$ represent valuable additions to this rare N-based Li superionic conductor family. Note that their electrochemical stability against Li metal was also theoretically suggested in a previous study.^[66]

Moreover, Li_7PSe_6 (bandgap 1.79 eV) decomposes at the anode into Li_3P and Li_2Se , both recognized for their excellent Li ionic conductivities.^[67,68] Thus, Li_7PSe_6 may form a stable, ionically conductive interphase with the Li metal anode, making it another promising SSE for the anode side.

On the cathode side, the phase equilibria of $\text{Li}_{10}\text{X}(\text{PS}_6)_2$ ($X = \text{Si}$, Ge , or Sn) (bandgap 2.27–2.46 eV), $\text{Li}_2\text{Mn}_{0.75}\text{Ta}_{0.5}\text{Sn}_{0.5}\text{S}_4$ (bandgap 2.95 eV), $\text{Li}_2\text{Zn}_{0.5}\text{TaS}_4$ (bandgap 2.92 eV) consist of S- or Se-based compounds. These compounds have the potential to

form ionically conductive but electronically insulating passivated glassy layers,^[67,69] supporting their suitability as SSEs at the cathode interface in solid-state battery systems.

These results indicate that $\text{Li}_{6.5}\text{Ta}_{0.5}\text{W}_{0.5}\text{N}_4$, $\text{Li}_{6.5}\text{Nb}_{0.5}\text{W}_{0.5}\text{N}_4$, and Li_7PSe_6 are promising SSEs for use at the anode interface, while $\text{Li}_{10}\text{X}(\text{PS}_6)_2$ ($X = \text{Si}$, Ge , or Sn), $\text{Li}_2\text{Mn}_{0.75}\text{Ta}_{0.5}\text{Sn}_{0.5}\text{S}_4$, and $\text{Li}_2\text{Zn}_{0.5}\text{TaS}_4$ are suitable for the cathode interface. Identifying these materials greatly enhances the options for designing effective SSEs in Li-ion batteries.

4. Conclusion

In this study, we developed a high-throughput screening model based on two structural factors, namely, D_{path} and D_{Li} , which can effectively identify Li superionic conductors ($\sigma_{\text{RT}} > 10^{-4}$ S cm^{-1}). This model was validated by examining the relationship between structural properties and σ_{RT} values in 132 experimentally available LICs. We demonstrated that the key characteristics of Li superionic conductors ($\sigma_{\text{RT}} > 10^{-4}$ S cm^{-1}) are the coexistence of sufficiently large diffusion pathways ($D_{\text{path}} > 1.00$ \AA) and a high-dimensional network of movable Li ions ($D_{\text{Li}} = 3$, or 2 for layered LICs). Using these criteria, we identified 33 potential Li-ion superionic conductors (Table S2, Supporting Information) from 21 686 LICs in the Materials Project database. After excluding 16 candidates containing expensive or toxic elements and four previously known conductors, we narrowed the list to 13 viable new candidates. And all these 13 candidates were confirmed as Li-ion superionic conductors through FPMD simulations, making them strong candidates for future experimental investigation.

Among 13 confirmed candidates, several new types of Li superionic conductors were identified. Notably, two N-containing materials (i.e., $\text{Li}_{6.5}\text{Ta}_{0.5}\text{W}_{0.5}\text{N}_4$ and $\text{Li}_{6.5}\text{Nb}_{0.5}\text{W}_{0.5}\text{N}_4$) were identified, which enrich the rare N-based Li superionic conductor family. $\text{Li}_2\text{Mo}_3\text{S}_4$, which shows the highest room-temperature Li ionic conductivity (6.24×10^{-2} S cm^{-1}), was further validated by FPMD (1 ns) and DeepMD (40 ns) simulations at room temperature. This exceptional conductivity is attributed to its unique structure of interconnected Mo_6S_8 clusters.

By considering electronic conductivity and electrochemical stability at the electrode interfaces, we identified several promising SSEs for solid-state Li-ion batteries: $\text{Li}_{6.5}\text{Ta}_{0.5}\text{W}_{0.5}\text{N}_4$, $\text{Li}_{6.5}\text{Nb}_{0.5}\text{W}_{0.5}\text{N}_4$, and Li_7PSe_6 for the anode interface, and $\text{Li}_{10}\text{X}(\text{PS}_6)_2$ ($X = \text{Si}$, Ge , or Sn), $\text{Li}_2\text{Mn}_{0.75}\text{Ta}_{0.5}\text{Sn}_{0.5}\text{S}_4$, and $\text{Li}_2\text{Zn}_{0.5}\text{TaS}_4$ for the cathode interface. $\text{Li}_{6.5}\text{Ta}_{0.5}\text{W}_{0.5}\text{N}_4$, $\text{Li}_{6.5}\text{Nb}_{0.5}\text{W}_{0.5}\text{N}_4$ exhibit excellent compatibility with the Li anode, remaining stable without decomposition. While Li_7PSe_6 decomposes at the anode and $\text{Li}_{10}\text{X}(\text{PS}_6)_2$, $\text{Li}_2\text{Mn}_{0.75}\text{Ta}_{0.5}\text{Sn}_{0.5}\text{S}_4$, and $\text{Li}_2\text{Zn}_{0.5}\text{TaS}_4$ decompose at the cathode, their decomposition products can form ionically conductive but electronically insulating passivating interphase layers on the electrodes, enhancing overall stability.

Li superionic conductors, such as those identified in this study, hold great promise in many applications. Those with wide bandgaps are especially promising for solid-state electrolytes for next-generation batteries, offering improved safety and stability over traditional liquid electrolytes. Notably, Li-ion content in some materials can be increased via aliovalent substitution, which could enhance their D_{Li} values. Therefore, LICs with $D_{\text{path}} > 1.00$ \AA but $D_{\text{Li}} < 3$ may be further optimized to be Li-ion

superionic conductors through appropriate Li content modification. Moreover, considering the similar diffusion of other metal ions, such as Na, K, and Zn, our screening model could likely be extended to explore superionic conductors for other metals. This study not only provides a highly accurate screening model for identifying Li superionic conductors, but also introduces several novel frameworks for designing new materials in this class.

Supporting Information

Supporting Information is available from the Wiley Online Library or from the author.

Acknowledgements

This work was supported in China by the Natural Science Foundation of Shandong Province (Grant No. ZR2020BM016) and the Shandong Laboratory of Advanced Materials and Green Manufacturing at Yantai (Grant No. AMGM2023A07), and in the USA by the NSF Center for the Advancement of Wearable Technologies (Grant No. 1849243).

Conflict of Interest

The authors declare no conflict of interest.

Data Availability Statement

The data that support the findings of this study are available in the supplementary material of this article.

Keywords

DFT calculations, high ionic conductivity, high-throughput screening, Li superionic conductors, solid-state batteries

Received: March 27, 2025

Published online:

- [1] M. Armand, J. M. Tarascon, *Nature* **2008**, 451, 652.
- [2] J. B. Goodenough, K. S. Park, *J. Am. Chem. Soc.* **2013**, 135, 1167.
- [3] R. Schmuch, R. Wagner, G. Hörpel, T. Placke, M. Winter, *Nat. Energy* **2018**, 3, 267.
- [4] J. B. Goodenough, Y. Kim, *Chem. Mater.* **2010**, 22, 587.
- [5] S. Randau, D. A. Weber, O. Kotz, R. Koerver, P. Braun, A. Weber, E. I. Tiffee, T. Adermann, J. Kulisch, W. G. Zeier, F. H. Richter, J. Janek, *Nat. Energy* **2020**, 5, 259.
- [6] D. H. S. Tan, A. Banerjee, Z. Chen, Y. S. Meng, *Nat. Nanotechnol.* **2020**, 15, 170.
- [7] T. Famprikis, P. Canepa, J. A. Dawson, M. S. Islam, C. Masquelier, *Nat. Mater.* **2019**, 18, 1278.
- [8] L. Kahle, A. Marcolongo, N. Marzari, *Energy Environ. Sci.* **2020**, 13, 928.
- [9] G. Adachi, N. Imanaka, S. Tamura, *Chem. Rev.* **2002**, 102, 2405.
- [10] C. W. Wang, K. Fu, S. P. Kammampata, D. W. McOwen, J. Samson, L. Zhang, G. T. Hitz, A. M. Nolan, E. D. Wachsman, Y. F. Mo, V. Thangadurai, L. B. Hu, *Chem. Rev.* **2020**, 120, 4257.
- [11] V. Thangadurai, S. Narayanan, D. Pinzar, *Chem. Soc. Rev.* **2014**, 43, 4714.
- [12] M. Menetrier, C. Estournes, A. Levasseur, K. Rao, *Solid State Ionics* **1992**, 53, 1208.
- [13] Y. Sun, K. Suzuki, S. Hori, M. Hirayama, R. Kanno, *Chem. Mater.* **2017**, 29, 5858.
- [14] Y. Kato, S. Hori, R. Kanno, *Adv. Energy Mater.* **2020**, 10, 2002153.
- [15] J. Goodenough, H. P. Hong, J. Kafalas, *Mater. Res. Bull.* **1976**, 11, 203.
- [16] S. Shi, L. Xu, C. Ouyang, Z. Wang, L. Chen, *Ionics* **2006**, 12, 343.
- [17] M. Lei, R. R. Yin, X. L. D. Ji, D. E. Jiang, *Adv. Funct. Mater.* **2024**, 34, 2410509.
- [18] H. J. Deiseroth, S. T. Kong, H. Eckert, J. Vannahme, C. Reiner, T. Zaiss, M. Schlosser, *Angew. Chem., Int. Ed.* **2008**, 47, 755.
- [19] S. Yubuchi, M. Uematsu, M. Deguchi, A. Hayashi, M. Tatsumisago, *ACS Appl. Energy Mater.* **2018**, 1, 3622.
- [20] Y. Zhao, L. L. Daemen, *J. Am. Chem. Soc.* **2012**, 134, 15042.
- [21] X. J. Lu, J. W. Howard, A. P. Chen, J. L. Zhu, S. Li, G. Wu, P. Dowden, H. W. Xu, Y. S. Zhao, Q. X. Jia, *Adv. Sci.* **2016**, 3, 1500359.
- [22] I. D. Brown, *Chem. Rev.* **2009**, 12, 6858.
- [23] M. Avdeev, M. Sale, S. Adams, R. P. Rao, *Solid State Ionics* **2012**, 225, 43.
- [24] B. He, S. T. Chi, A. J. Ye, P. H. Mi, L. W. Zhang, B. W. Pu, Z. Y. Zou, Y. B. Ran, Q. Zhao, D. Wang, W. Q. Zhang, J. T. Zhao, S. Adams, M. Avdeev, S. Q. Shi, *Sci. Data* **2020**, 7, 151.
- [25] L. Kahle, A. Marcolongo, N. Marzari, *Phys. Rev. Mater.* **2018**, 2, 065405.
- [26] F. L. Yang, E. C. D. Santos, X. Jia, R. Sato, K. Kisu, Y. Hashimoto, S. I. Orimo, H. Li, *Nano Mater. Sci.* **2024**, 6, 256.
- [27] Y. Wang, W. D. Richards, S. P. Ong, L. J. Miara, J. C. Kim, Y. F. Mo, G. Ceder, *Nat. Mater.* **2015**, 14, 1026.
- [28] Y. Zhang, X. F. He, Z. Q. Chen, Q. Bai, A. M. Nolan, C. A. Roberts, D. Banerjee, T. Matsunaga, Y. F. Mo, C. Ling, *Nat. Commun.* **2019**, 10, 5260.
- [29] X. F. He, Y. Z. Zhu, Y. F. Mo, *Nat. Commun.* **2016**, 8, 15893.
- [30] A. D. Sendek, E. D. Cubuk, E. R. Antoniuk, G. Cheon, Y. Cui, E. I. Reed, *Chem. Mater.* **2019**, 31, 342.
- [31] E. D. Cubuk, A. D. Sendek, E. J. Reed, *J. Chem. Phys.* **2019**, 150, 214701.
- [32] A. D. Sendek, Q. Yang, E. D. Cubuk, K. A. N. Duerloo, Y. Cui, E. J. Reed, *Energy Environ. Sci.* **2017**, 10, 306.
- [33] S. Mui, J. Voss, R. Schlem, R. Koerver, S. J. Sedlmaier, F. Maglia, P. Lamp, W. G. Zeier, Y. Shao-Horn, *iScience* **2019**, 16, 270.
- [34] X. F. He, Q. Bai, Y. S. Liu, A. M. Nolan, C. Ling, Y. F. Mo, *Adv. Energy Mater.* **2019**, 9, 1902078.
- [35] S. Wang, Y. S. Liu, Y. F. Mo, *Angew. Chem., Int. Ed.* **2023**, 62, 202215544.
- [36] Z. T. Liu, P. H. Chien, S. Wang, S. W. Song, M. Lu, S. Chen, S. M. Xia, J. Liu, Y. F. Mo, H. L. Chen, *Nat. Chem.* **2024**, 16, 1584.
- [37] A. Jain, G. Hautier, S. P. Ong, C. J. Moore, C. C. Fischer, K. A. Persson, G. Ceder, *Phys. Rev. B* **2011**, 84, 045115.
- [38] G. Kresse, J. Furthmüller, *Comp. Mater. Sci.* **1996**, 6, 15.
- [39] G. Kresse, J. Furthmüller, *Phys. Rev. B* **1996**, 54, 11169.
- [40] G. Kresse, D. Joubert, *Phys. Rev. B* **1999**, 59, 1758.
- [41] J. P. Perdew, A. Ruzsinszky, G. I. Csonka, O. A. Vydrov, G. E. Scuseria, L. A. Constantin, X. L. Zhou, K. Burke, *Phys. Rev. Lett.* **2008**, 100, 136406.
- [42] X. F. He, Y. Z. Zhu, A. Epstein, Y. F. Mo, *npj Comput. Mater.* **2018**, 4, 18.
- [43] S. Nose, *Prog. Theor. Phys. Suppl.* **1991**, 103, 1.
- [44] G. Hautier, C. Fischer, V. Ehrlicher, A. Jain, G. Ceder, *Inorg. Chem.* **2010**, 50, 656.
- [45] K. Okhotnikov, T. Charpentier, S. Cadars, *J. Cheminf.* **2016**, 8, 17.
- [46] H. Wang, L. Zhang, J. Han, E. Weinan, *Comput. Phys. Commun.* **2018**, 228, 178.

- [47] S. Plimpton, *J. Comput. Phys.* **1995**, *117*, 1.
- [48] D. P. Kingma, J. Ba, arXiv.1412.6980, **2017**.
- [49] S. P. Ong, W. D. Richards, A. Jain, G. Hautier, M. Kocher, S. Cholia, D. Gunter, V. L. Chevrier, K. A. Persson, G. Ceder, *Comp. Mater. Sci.* **2013**, *68*, 314.
- [50] T. F. Willems, C. H. Rycroft, M. Kazi, J. C. Meza, M. Haranczyk, *Microporous Mesoporous Mater* **2012**, *149*, 134.
- [51] R. L. Martin, B. Smit, M. Haranczyk, *J. Chem. Inf. Model.* **2012**, *52*, 308.
- [52] M. B. Salamon, Springer, Berlin, Heidelberg, **2011**, 15, 175–199.
- [53] W. Dieterich, P. Fulde, I. Peschel, *Adv. Phys.* **2006**, *29*, 527.
- [54] K. J. Jun, Y. Chen, G. Wei, X. C. Yang, G. Ceder, *Nat. Rev. Mater.* **2024**, *9*, 887.
- [55] A. Bondi, *J. Phys. Chem.* **1964**, *68*, 441.
- [56] J. Peng, Y. H. Liu, Y. Pan, J. J. Wu, Y. Q. Su, Y. Q. Guo, X. J. Wu, C. Z. Wu, Y. Xie, *J. Am. Chem. Soc.* **2020**, *142*, 18645.
- [57] K. J. Jun, Y. Z. Sun, Y. H. Xiao, Y. Zeng, R. H. Kim, H. Y. Kim, L. J. Miara, D. M. Im, Y. Wang, G. Ceder, *Nat. Mater.* **2022**, *21*, 924.
- [58] Q. D. Wang, Y. N. Zhou, X. L. Wang, H. Guo, S. P. Gong, Z. P. Yao, F. T. Wu, J. L. Wang, S. Ganapathy, X. D. Bai, B. H. Li, C. L. Zhao, J. Janek, M. Wagemaker, *Nat. Commun.* **2024**, *15*, 1050.
- [59] S. Wang, Q. Bai, A. M. Nolan, Y. S. Liu, S. Gong, Q. Sun, Y. F. Mo, *Angew. Chem., Int. Ed.* **2019**, *58*, 8039.
- [60] S. Wang, L. Zhao, Y. Dong, H. Zhu, Y. Yang, H. Xu, B. Wang, Y. Yuan, Y. Ren, X. Huang, W. Quan, Y. Li, Y. Huang, C. Settens, Q. He, Y. Sun, H. Wang, Z. Xiao, W. Liu, X. Xiao, R. Fu, Q. Li, Y. Chu, Z. Zhang, Q. Liu, A. Minor, J. Zhang, Z. Tang, J. Li, *Energy Environ. Sci.* **2023**, *16*, 241.
- [61] Y. Chen, Z. Wang, X. Li, X. Yao, C. Wang, Y. Li, W. Xue, D. Yu, S. Y. Kim, F. Yang, A. Kushima, G. Zhang, H. Huang, N. Wu, Y.-W. Mai, J. B. Goodenough, J. Li, *Nature* **2020**, *578*, 251.
- [62] A. M. Nolan, Y. Z. Zhu, X. F. He, Q. Bai, Y. F. Mo, *Joule* **2018**, *2*, 2016.
- [63] M. Marsman, J. Paier, A. Stroppa, G. Kresse, *J. Phys.:Condens. Matter* **2008**, *20*, 064201.
- [64] S. P. Ong, L. Wang, B. Kang, G. Ceder, *Chem. Mater.* **2008**, *20*, 1798.
- [65] P. F. Ren, X. D. Wang, B. Huang, Z. Liu, R. P. Liu, *J. Energy Storage* **2024**, *82*, 110200.
- [66] Y. Z. Zhu, X. F. He, Y. F. Mo, *Adv. Sci.* **2017**, *4*, 1600517.
- [67] F. Mizuno, A. Hayashi, K. Tadanaga, M. Tatsumisago, *Solid State Ionics* **2006**, *177*, 2721.
- [68] N. Wu, Y. Li, A. Dolocan, W. Li, H. Xu, B. Xu, N. S. Grundish, Z. Cui, H. Jin, J. B. Goodenough, *Adv. Funct. Mater.* **2020**, *30*, 2000831.
- [69] S. P. Ong, Y. F. Mo, W. D. Richards, L. Miara, H. S. Lee, G. Ceder, *Energy Environ. Sci.* **2013**, *6*, 148.